# Synthesis of a Highly Stable Pd@CeO$_2$ Catalyst for Methane Combustion with the Synergistic Effect of Urea and Citric Acid

Guohui Cai, Wei Luo, Yihong Xiao, Yong Zheng, Fulan Zhong, Yingying Zhan,* and Lilong Jiang

National Engineering Research Center of Chemical Fertilizer Catalyst, College of Chemical Engineering, Fuzhou University, Gongye Road No. 523, Fuzhou 350002, Fujian, P. R. China

S *Supporting Information*

ABSTRACT: Making use of synergy between urea and citric acid, a core−shell Pd@CeO$_2$ catalyst with spherical morphology was facilely synthesized by a hydrothermal method. The formation mechanism of the core−shell structure in the presence of citric acid and hydrogen peroxide was studied. Results showed that the Pd@CeO$_2$ catalyst exhibited high catalytic activity in methane oxidation. Pd nanoparticles were well stabilized by CeO$_2$ shell encapsulation, resulting in high stability of the catalyst. A high CH$_4$ conversion of 99% was retained after 50 h on-stream reaction at 500 °C. Additionally, many tiny pores on the CeO$_2$ shell surface were beneficial for the full contact between reactants and active components. Pd nanoparticles were highly dispersed inside the shell, improving the utilization efficiency of active components. The results also demonstrated that the Pd species in the catalyst existed in the form of oxidation state, mainly in PdO (ca. 66.6%), which played an essential part in methane combustion.
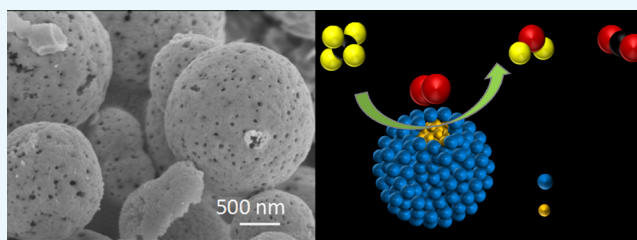
1. INTRODUCTION

Methane is the main component of natural gas, which possesses the advantages such as high practicability and low price. It produces less carbon dioxide per unit of energy than diesel or gasoline, and is known as a "green" alternative to these fuels. Thus, it is more suitable for acting as a promising candidate for automotive fuels.[1,2] However, the direct emission of a small amount of unburned methane will cause a much higher greenhouse effect than carbon dioxide.[3] Besides, as composed with other hydrocarbons, the C−H bond (∼400 kJ mol^{-1}) in CH$_4$ is more stable and difficult to be activated.[4,5] Therefore, it is vital to exploit an effective method to reduce methane emissions into the atmosphere.

So far, methane catalytic combustion is considered to be the most effective, economical, simple, and clean method to reduce residual methane in vehicle exhaust. In order to control such emissions, various catalysts for methane catalytic combustion were studied and prepared, such as precious metals,[6−8] perovskites,[9−11] and hexaaluminates.[12,13] In general, non-noble metal catalysts show high activity for methane oxidation only under the conditions of high temperature, high pressure, or other harsh terms, which will result in the increase of pollutants and more energy consumption. In contrast, the noble metal catalysts, especially the supported palladium catalysts,[14,15] exhibit high catalytic activity for methane complete combustion.[16,17]

Reversible adsorption and desorption of oxygen occur in the process of methane catalytic combustion over the supported Pd catalysts. In addition, the nature of support is crucial for the catalyst properties, which are closely related to the dispersity of Pd species on the support as well as the interaction between Pd species and support.[18−21] One suitable support is beneficial for the stability of the active PdO phase, preventing the thermal decomposition and sintering of PdO under high temperature.[22,23] Meanwhile, catalyst carriers also affect the ability of Pd to adsorb oxygen,[24] in turn affecting the performance of the catalyst. Therefore, high adsorption capacity to oxygen and good oxidation−reduction properties of the catalyst carriers will be beneficial to the enhancement of the catalyst performance.

CeO$_2$ has been extensively used to act as a carrier for noble metal nanoparticles because of the excellent performance of CeO$_2$, such as good ability to disperse active components, structural stability,[25,26] and superior ability to store and release oxygen.[27,28] Among, Pd/CeO$_2$ catalysts are usually prepared to investigate the catalytic combustion properties of methane.[29,30] However, the low-temperature catalytic activity and thermal stability over the Pd-based catalysts were insufficient in the presence of a large amount of water vapor and carbon dioxide. In recent years, many research studies have shown that the reasonable design of the Pd species-metal oxide (MO) interface is an effective method to improve the performance of Pd-based catalysts, especially the core−shell nanostructured Pd@MO catalysts have attracted extensive attention.[31−35] Wang et al. developed the self-assembly of CeO$_2$ on a variety of Pd nanoparticles by using the biological molecule L-arginine

as a sealing agent.[33] Compared with other CeO_2 supported noble metal materials (NM/CeO_2), $NM@CeO_2$ with core−shell nanostructures significantly improved the catalytic activity and stability of the catalysts, which may be derived from the protection of precious metals by the CeO_2 shell preventing them from being transformed in large quantities during long catalytic processes or under high temperatures. $Pd@CeO_2$ core−shell nanocomposites by using tetrahydrofuran as solvents were synthesized and grafted onto Al_2O_3 to obtain $Pd@CeO_2/Al_2O_3$ catalysts by Cargnello et al., which demonstrated that the sample showed high activity in methane catalytic combustion and the chemical state of Pd nanoparticles could be stabilized through the strong interactions between CeO_2 and Pd.[34] As mentioned above, it can be seen that the formation of such a $Pd@CeO_2$ core−shell structure shows unique advantages in improving the performance of the catalyst. However, at present, the synthesis process of $Pd@CeO_2$ catalysts is relatively complicated, the use of reagents as surfactants or solvents is not environmentally friendly, and challenges still exist in the regulation of catalyst morphology. Therefore, it is urgently needed and meaningful to develop a green, simple, and suitable synthesis method to obtain $Pd@CeO_2$ catalysts with core−shell nanostructures and specific morphology. Meanwhile, the formation of strong interactions between CeO_2 and Pd particles via the reducible property of CeO_2 is beneficial to prevent precious metals from migrating and agglomerating at a high temperature, and the protective layer formed by the CeO_2 shell is good for improving the stability of the catalyst. These promotion effects are important to the methane combustion reaction.

Herein, one core−shell nanostructured $Pd@CeO_2$ catalyst with spherical morphology was rationally designed for methane catalytic combustion through a facile hydrothermal method with citric acid as a complexing agent, hydrogen peroxide as an oxidant, and urea used to adjust the formation rate of hydrogen peroxide radicals. The influences of the catalyst morphology and the chemical state of Pd species on the catalytic activity were discussed, as well as the catalytic mechanism. It was found that the core−shell nanostructure formed through a CeO_2 shell encapsulating Pd nanoparticles played an important role in the stabilization of the catalyst structures. In addition, PdO acting as the main active sites in the catalyst dominated the methane catalytic combustion reaction. The study provides a new way to prepare the core−shell structure catalyst.

2. RESULTS AND DISCUSSION

2.1. Morphology Analysis. The scanning electron microscopy (SEM) images of the catalysts prepared by different synthetic methods were shown and compared in Figure 1. I−Pd/CeO_2-600 exhibited irregular spherical morphology (Figure 1A), with small particle size, uneven distribution, and rough surface, while no specific morphology was observed for C−Pd/CeO_2-600 (Figure 1B). For the catalyst prepared through the hydrothermal method, it had relatively regular spherical morphology (Figure 1C,D), which was desirable in practical applications for methane combustion. Meanwhile, it can be seen that the hydrothermal treatment time has an obvious influence on the morphology as shown in Figure S1. For the catalyst prepared under 18−24 h hydrothermal treatment, relatively regular spherical particles were obtained. As shown in Figure S1D, the particle size for H−$Pd@CeO_2$-600(24) was around 1−2 μm for smaller particles and was around 3−4 μm for the larger ones. The
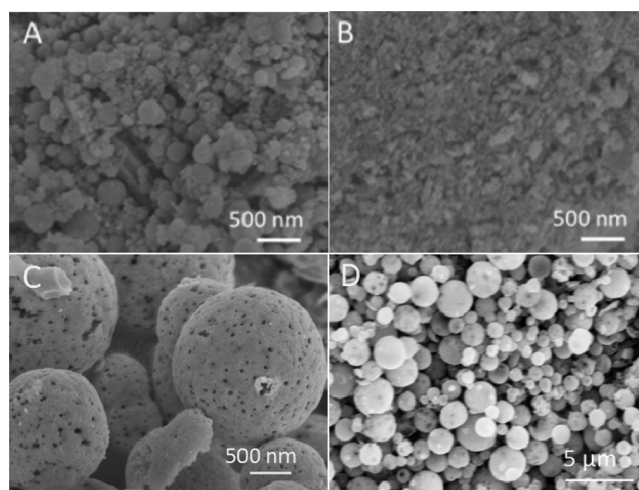

Figure 1. SEM images of I−Pd/CeO_2-600 (A), C−Pd/CeO_2-600 (B), and H−$Pd@CeO_2$-600(24) (C,D).

microspheres may be self-assembled from the secondary particles formed by primary particles under hydrothermal conditions. In addition, obvious holes were formed on the surface of H−$Pd@CeO_2$-600(24), which may be due to the escape of the gas produced by the decomposition of organic compounds.

As mentioned in the SEM analysis of Figure 1C,D, the microspheres with a size in the range of 1−2 μm prevailed in H−$Pd@CeO_2$-600(24). In order to have an insight into the state of palladium species, the transmission electron microscopy (TEM) and high resolution TEM (HRTEM) analyses for those separated from the H−$Pd@CeO_2$-600(24) microspheres were conducted, and the results were shown in Figure 2A−D. It can be found that the individual palladium particles were encapsulated by CeO_2 particles, indicating the formation of the core−shell nanostructure with the PdO particle diameter of ca. 8.7 nm. The lattice fringe spacings of core and shell were 0.26 and 0.31 nm, which were ascribed to the (101) crystal plane of PdO and the (111) crystal plane of CeO_2 with the cubic fluorite structure, respectively.[36,37] Combining with SEM characterization results, it was considered that the prepared catalyst consisted of microspheres which were secondarily assembled by CeO_2 shell wrapping PdO nanoparticles. As shown in Figure 2E−H, high-angle annular dark-field scanning transmission electron microscopy (HAADF-STEM) image and energy-dispersive spectrometry (EDS) mapping analysis further confirmed the core−shell structured $Pd@CeO_2$ nanoparticles with Pd particles uniformly distributing in the core were successfully obtained through the hydrothermal method.

2.2. Structural Properties. The results of wide-angle X-ray diffraction (XRD) for the catalysts prepared with different methods and hydrothermal time are displayed in Figure 3A,B. The diffraction peaks at 2θ of 28.5°, 33.1°, 47.5°, 56.3°, 59.1°, 69.4°, 76.7°, 79.1°, 88.4°, and 95.4°, which were detected all over the samples, were consistent with the characteristic peaks of the CeO_2 species with cubic fluorite structures.[38] Except H−Pd/CeO_2-600(6), no diffraction peaks attributable to palladium species were observed in other samples because of the good dispersion and low loading amount beyond the detection limit. H−Pd/CeO_2-600(6) exhibited an obvious diffraction peak near 33.9° ascribed to tetragonal PdO(101),[15,28] indicating that increasing hydrothermal treatment time was conducive to the high dispersion of Pd species. In combination
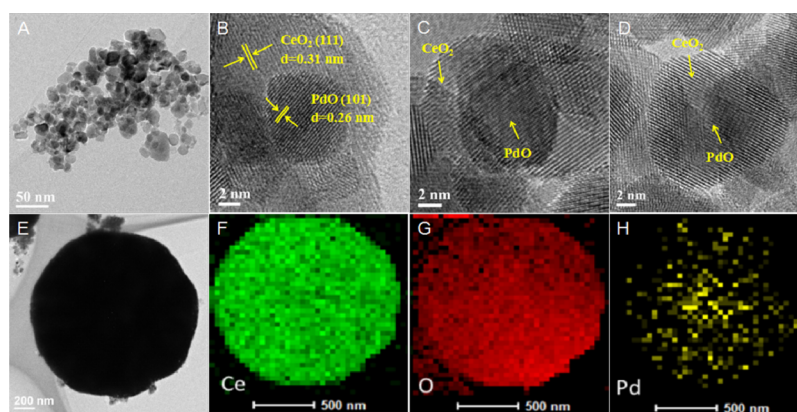
Figure 2. TEM image (A), HRTEM image (B−D), HAADF-STEM image (E), and EDS mapping analysis (F−H) of H−Pd@CeO$_2$-600(24).
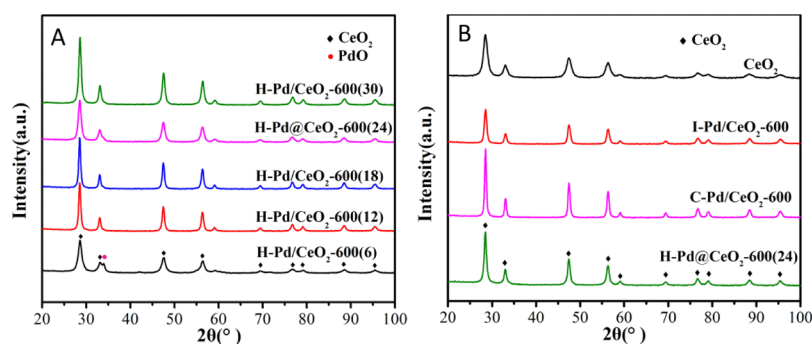
Figure 3. XRD spectra of (A) H−Pd/CeO$_2$-600(t) and (B) CeO$_2$, H−Pd@CeO$_2$-600(24), I−Pd/CeO$_2$-600, and C−Pd/CeO$_2$-600.
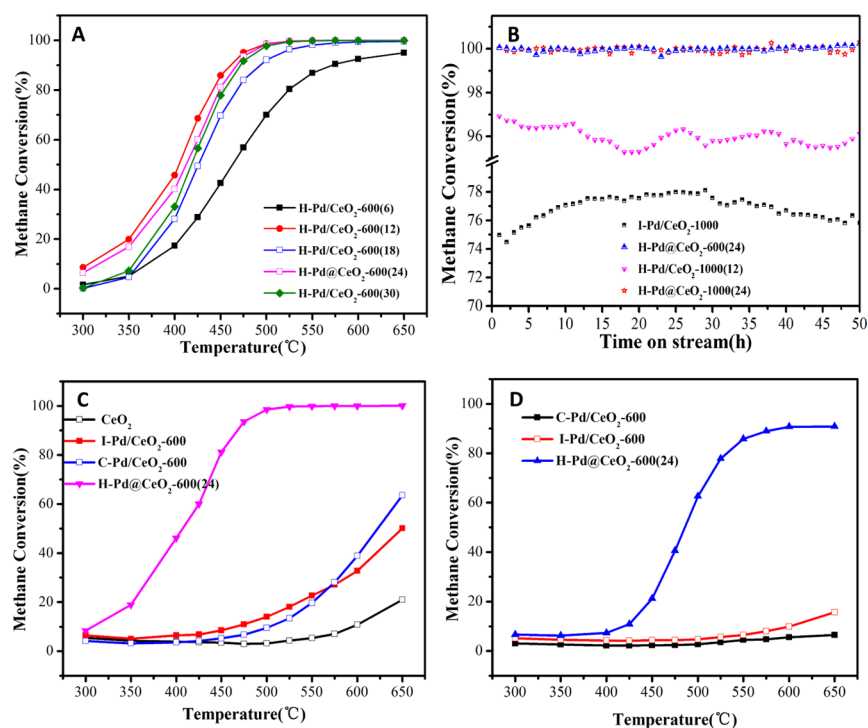
Figure 4. (A) is CH$_4$ conversion over H−Pd/CeO$_2$-600(t). (B) is stability test of H−Pd@CeO$_2$-1000(12), H−Pd@CeO$_2$-1000(24), H−Pd@CeO$_2$-600(24), and I−Pd/CeO$_2$-1000. (C,D) are CH$_4$ conversion over the catalysts synthesized by different methods under dry feed condition and wet feed condition (15% extra water), respectively. Dry feed: 2 vol % CH$_4$, 4 vol % O$_2$, and 20 vol % CO$_2$ in N$_2$ as balance gas; GHSV of 100 000 mL h^{-1} g^{-1}.

with SEM images, it was rational to conclude that PdO particles could not be well coated by the CeO$_2$ shell for H−

Pd/CeO$_2$-600(6) so that the PdO particles were aggregated and crystallized into larger particles. On the basis of the results

of CO pulse chemisorption (Table S1), it could be found H−Pd@CeO$_2$-600(24) displayed a higher dispersion than other samples, indicating that the structure of CeO$_2$ shell wrapping Pd cores in H−Pd@CeO$_2$-600(24) was favorable for promoting the dispersion of Pd species.[39] The conclusion was in agreement with the analysis of HAADF-STEM.

2.3. Catalytic Performance. The catalytic performance of the H−Pd/CeO$_2$-600(t) catalysts synthesized under different hydrothermal treatment times is depicted and compared in Figure 4A. It is noted that the H−Pd/CeO$_2$-600(t) (t = 12−30) catalysts exhibited no distinct difference in catalytic activities, while they presented superior catalytic performances than the H−Pd/CeO$_2$-600(6) catalyst. The consequence may result from the high dispersion of active nanoparticles with smaller particle sizes for H−Pd/CeO$_2$-600(t) (t = 12−30) catalysts, which was confirmed from XRD analysis (Figure 3A). For the sake of further investigating the influence of morphology on catalytic activity, activity, and stability tests were accomplished for the H−Pd/CeO$_2$-1000(12) and H−Pd@CeO$_2$-1000(24) catalysts with a different morphology which was selected as representatives. The CH$_4$ conversion over H−Pd@CeO$_2$-1000(24) and H−Pd/CeO$_2$-1000(12) was maintained ∼99 and ∼95%, respectively, after reaction for 50 h at 500 °C (Figure 4B). In combination with the stability result of the H−Pd@CeO$_2$-600(24) catalyst (Figure 4B), it can be concluded that H−Pd@CeO$_2$-600/1000(24) possessed superior temperature thermal stability than H−Pd/CeO$_2$-1000(12). This result may be due to the relatively regular morphology for H−Pd@CeO$_2$-600/1000(24), which was beneficial to the mass and heat transfer of the catalysts,[40] as well as anti-sintering of the nanoparticles.

As displayed in Figure 4C and Table 1, H−Pd@CeO$_2$-600(24) demonstrated superior catalytic performance than I−

Table 1. Comparison of Methane Combustion Performance of Catalysts Prepared by Different Synthetic Methods

catalyst	T_{10} (°C)	T_{50} (°C)	T_{90} (°C)
CeO$_2$	595		
I−Pd/CeO$_2$-600	466	649	
C−Pd/CeO$_2$-600	504	622	
H−Pd@CeO$_2$-600(24)	307	406	465
I−Pd/CeO$_2$-1000	364	463	538
C−Pd/CeO$_2$-1000	528		
H−Pd@CeO$_2$-1000(24)	308	408	467

Pd/CeO$_2$-600 and C−Pd/CeO$_2$-600, which indicated that the activities for CH$_4$ combustion varied with the synthesis methods. Among them, the T_{99} of H−Pd@CeO$_2$-600(24) catalyst was as low as 500 °C, while I−Pd/CeO$_2$-600 and C−Pd/CeO$_2$-600 showed negligible catalytic activity when the reaction temperature was below 500 °C. Figure S2A shows the catalytic performance of the samples calcined at 1000 °C. It can be seen that the catalytic activities decreased in the order H−Pd@CeO$_2$-1000(24) > I−Pd/CeO$_2$-1000 > C−Pd/CeO$_2$-1000.

The results displayed that H−Pd@CeO$_2$-600/1000(24) catalysts exhibited similar activity. For I−Pd/CeO$_2$-T catalysts, I−Pd/CeO$_2$-1000 exhibited better activity than I−Pd/CeO$_2$-600, which demonstrated that the high-temperature heat treatment was beneficial to the promotion of its catalytic activity. Besides, the methane conversion at 500 °C for I−Pd/CeO$_2$-1000 fluctuated between 74 and 78% during 50 h on

stream reaction. Whereas high-temperature calcination was unfavorable to the catalytic activity for the catalyst synthesized through a coprecipitation method. The consequence further provided evidence that H−Pd@CeO$_2$-T(24) demonstrated higher thermal stability than I−Pd/CeO$_2$-T and C−Pd/CeO$_2$-T. The enhanced stability of noble metal nanoparticles through the encapsulation of the CeO$_2$ shell have also been reported in previously reported NM@CeO$_2$ core@shell nanostructures.[41,42] Additionally, H−Pd@CeO$_2$-600/1000(24) also exhibited good performance in comparison with those Pd-based catalysts previously reported. The T_{90} value for H−Pd@CeO$_2$-600/1000(24) at a space velocity of 100 000 mL h^{-1} g^{-1} was about 465 °C, which is lower than T_{90} (545 °C) for PdO/CeO$_2$@HZSM-5 operated at a low space velocity of 30 000 mL h^{-1} g^{-1}.[43]

The influence of H$_2$O on the catalytic activities of the catalysts was also investigated in the presence of 15 vol % H$_2$O. Comparing the result of Figure 4D with that in Figure 4C, it can be found that the presence of 15 vol % water vapor had an inhibitory effect on the performance of the catalysts regardless of the synthesis methods. Ciuparu and Pfefferle pointed out that when the active sites existed in oxidation states, the introduction of water could significantly inhibit the performance of the catalyst for methane combustion.[44] Gao et al. reported that the surface-active sites over Pd/Al$_2$O$_3$ catalysts were covered by hydroxyl groups in the presence of water, resulting in the formation of inactive Pd(OH)$_2$, thus the poisoning and inactivation of the active sites.[45] Gao et al. also pointed out that the reactivation effect with N$_2$ was superior to that with air after removal of water, which could be explained by that Pd(OH)$_2$ decomposed into PdO in the N$_2$ feed but PdO$_2$ in the air and PdO$_2$ species was normally considered to be less active than PdO species. Therefore, it could be inferred that the active sites on the as-prepared catalysts in this work might exist mainly in the Pd oxidation states rather than the metallic states, thus the catalytic activities were restricted by water.

In addition, considering that CO$_2$ was also the main product of methane catalytic combustion, the influence of CO$_2$ on the catalytic performance was also discussed. CO$_2$ temperature-programmed desorption (CO$_2$-TPD) curves of the catalyst are shown in Figure S2B. It was clear that the desorption temperature of CO$_2$ increased in the sequence of H−Pd@CeO$_2$-600(24) < I−Pd/CeO$_2$-600 < C−Pd/CeO$_2$-600. The lower desorption temperature and stronger peak intensity of H−Pd@CeO$_2$-600(24) indicated that H−Pd@CeO$_2$-600(24) presented weaker basicity strength but a higher amount of weakly basic sites, demonstrating that the catalyst surface had abundant active sites for CO$_2$ adsorption. The result demonstrated that the strength of catalyst surface basicity had an obvious effect on the catalytic activity. The existence of strong basicity sites was conducive to the competitive adsorption of CO$_2$ on the catalyst surface, but not beneficial to the methane activation. Therefore, H−Pd@CeO$_2$-600(24) with the weaker strength of catalyst surface basicity demonstrated higher catalytic activity. On the other hand, because the desorption temperature of CO$_2$ was all lower than 300 °C, it could be speculated that CO$_2$ had no obvious effect on the activities of the series of catalysts.

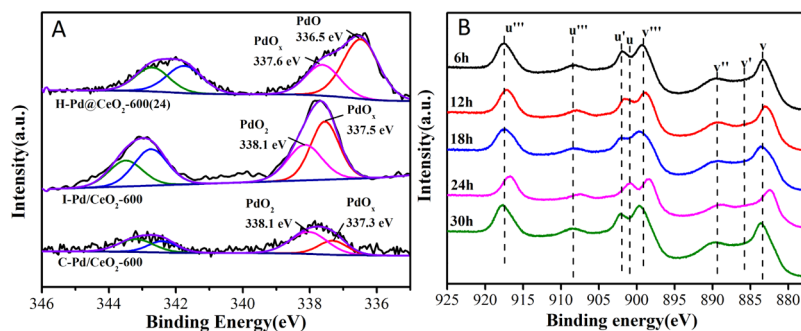**2.4. X-ray Photoelectron Spectroscopy Analysis.** Chemical states and distribution of Pd species on the catalysts prepared by different methods were analyzed by X-ray photoelectron spectroscopy (XPS). As shown in Figure 5A,

Figure 5. (A) Pd 3d XPS spectra of the catalysts prepared by different methods and (B) Ce 3d XPS spectra of H−Pd/CeO$_2$-600(t) catalysts.

two components of Pd species were detected over all of the samples. The Pd 3d$_{5/2}$ peak at 336.5 eV is assigned to the PdO species, the peaks at 337.3−337.6 and 338.1 eV can be attributed to the PdO$_x$ (1 < x < 2) and PdO$_2$ species, respectively,[28,46,47] indicating that only palladium oxide species were present which were normally considered to act as active sites in CH$_4$ combustion. This result confirmed that the reason for the activity difference of the catalysts in water-bearing systems was that the main active species on the surface of the catalysts were oxidized palladium species. As noted in Table 2,

Table 2. Analysis of Surface Pd Species of the Catalysts Derived from XPS Spectra

sample	peak name	peak BE (eV)	content (%)
H−Pd@CeO$_2$-600(24)	PdO	336.5	66.6
	PdO$_x$	337.6	33.4
I−Pd/CeO$_2$-600	PdO$_x$	337.5	59.3
	PdO$_2$	338.1	40.7
C−Pd/CeO$_2$-600	PdO$_x$	337.3	32.6
	PdO$_2$	338.1	67.4

the content of Pd^{2+} reached 66.6% for H−Pd@CeO$_2$-600(24), indicating that it has more palladium species with +2 valence, while Pd species on I−Pd/CeO$_2$-600 and C−Pd/CeO$_2$-600 mainly existed in the form of PdO$_x$ and PdO$_2$. Among the samples, H−Pd@CeO$_2$-600(24) possessed higher Pd^{2+} content, which was in line with the higher catalytic performance. The result substantiated that the catalytic activities may be mainly affected by the active PdO and PdO$_x$ species for methane combustion, whereas the contribution of PdO$_2$ species was much smaller than those of PdO and PdO$_x$ species.

Figure 5B shows the Ce 3d spectra of H−Pd/CeO$_2$-600(t) catalysts. The characteristic peaks of Ce 3d$_{5/2}$ and Ce 3d$_{3/2}$ were labeled as u and v, respectively. The label u′ and v′ peaks were corresponding to Ce^{3+}, whereas the peaks denoted by u, u″, u‴, v, v″ and v‴ belonged to Ce^{4+}.[48] As shown in Table S2, the Ce^{4+}/Ce^{3+} ratios over all of the catalysts were ranging from 6.9 to 21.3, demonstrating that Ce was mostly in a +4 oxidation state. The amount of Ce^{3+} on the surface of H−Pd@CeO$_2$-600(24) was relatively higher. This brought about more oxygen vacancy,[49] which would also boost the catalytic activity for CH$_4$ combustion. The results mentioned above suggested that the core−shell structure of Pd@CeO$_2$ provided more accessible active sites for the reactant (CH$_4$).

2.5. Redox Properties. Figure 6A shows hydrogen temperature-programmed reduction (H$_2$-TPR) profiles of catalysts prepared by different methods. One broad peak at 600−800 °C was observed on the three catalysts, which could be assigned to the reduction of CeO$_2$ lattice oxygen.[50] On the basis of the XPS results, the positive peak centered at 100−300 °C of I−Pd/CeO$_2$-600 and C−Pd/CeO$_2$-600 was assigned to the reduction of Pd species in the oxidation state (PdO or PdO$_2$). The reduction temperature of Pd species on C−Pd/CeO$_2$-600 was obviously higher, which could be attributed to the higher amount of PdO$_2$, making it relatively difficult to be reduced. For H−Pd@CeO$_2$-600(24), a negative peak at ca. 77 °C could be attributed to the decomposition of PdH$_x$ formed by the chemical adsorption of H$_2$ by metallic palladium.[51] Low-temperature H$_2$-TPR profiles (Figure 6B) showed that H−Pd@CeO$_2$-600(24) appeared an obvious H$_2$ consumption peak at 10−40 °C, corresponding to the reduction of PdO and PdO$_x$ (1 < x < 2) species as well as the formation of PdH$_x$ species. The results indicated that the reduction trend of Pd species over different catalysts was as follows: H−Pd@CeO$_2$-600(24) > I−Pd/CeO$_2$-600 > C−Pd/CeO$_2$-600. Combined
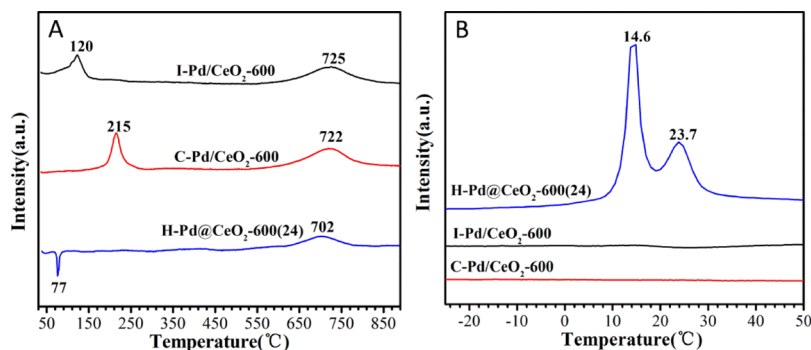
Figure 6. H$_2$-TPR profiles in the range of 40−900 °C (A) and −30 to 50 °C (B) of the catalysts prepared by different methods.

with the activity results, the reducibility of the catalysts was in agreement with the trend in catalytic activity, evidencing that higher reduction ability would profit CH_4 activation.

2.6. Synthesis Mechanism and Reaction Process. A possible synthesis mechanism of $H-Pd@CeO_2$-600(24) was proposed as described in Figure 7. The surface of
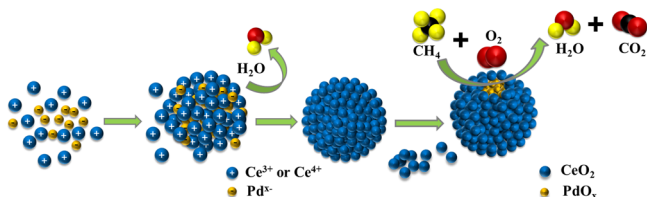
Figure 7. Schematic of the formation of core−shell structure and CH_4 oxidation over the catalyst $H-Pd@CeO_2$-T.

presynthesized Pd colloidal particles which was negatively charged could adsorb Ce^{3+}, and the −COOH group of citric acid in the system would also bind to Ce^{3+} ions. Urea was slowly hydrolyzed under hydrothermal conditions and promoted the decomposition of H_2O_2 into hydrogen peroxide ions $[HO_2^-]$ or peroxy hydrogen radicals $[HO_2^\bullet]$. During this process, part of Ce^{3+} ions was oxidized to Ce^{4+} ions, forming $Ce(OH)_3OOH$, which was further condensed and dehydrated to form CeO_2. In addition, within a certain period of hydrothermal time, the reaction became more sufficient with treatment time. Through the synergy of citric acid, CeO_2 formed a thicker and thicker coating around Pd particles, hence larger and larger nanoparticles. When the reaction time was insufficient, it failed to hydrolyze all cerium ions into hydroxides and form CeO_2. Part of the cerium ions which were complexed with citric acid could only form CeO_2 during the postcalcination treatment, resulting in irregular morphology. Too long a reaction time might result in the desorption of the formed small crystals or crystal nucleus, or the formation of larger particles because of the overlapping or lateral connection of the surface nucleation, thus causing the formation of irregular morphology. The mechanism demonstrated that the control of hydrothermal reaction time played an important part in a attaining regular spherical structure.

When the reaction atmosphere passed through the pores on the CeO_2 surface of the catalyst, CH_4 reacted with the encapsulated active Pd species. As mentioned above, the presence of regular spherical CeO_2 shells effectively prevented the agglomeration and sintering of Pd species to form large particles and facilitated the dispersion of Pd species on the carrier. Therefore, more active Pd species are involved in the methane combustion reaction, leading to the enhancement of the catalytic activity.

3. CONCLUSIONS

In conclusion, using the synergy between urea and citric acid, a core−shell structured $Pd@CeO_2$ catalyst with uniform spherical morphology was successfully synthesized by a green and facile hydrothermal method. The active Pd species in the catalyst mainly existed in the form of PdO accompanied by the presence of some PdO_x ($1< x < 2$) oxides, and the active Pd species were highly dispersed inside the spherical CeO_2 shell. The core−shell structure stabilized the active PdO particles in the catalyst and improved the utilization efficiency of the active component. The $Pd@CeO_2$ catalyst exhibited high stability,

which maintained 99% methane conversion after continuous reaction for 50 h at 500 °C. This work provided a new idea for the further development of novel methane combustion catalysts.

4. EXPERIMENTAL SECTION

4.1. Synthesis of Catalysts. The $Pd@CeO_2$ catalysts were prepared through a hydrothermal method as follows. The preparation of the Pd precursor was according to the reports by Wang[33] and Xia.[52] 108 mg of polyvinyl pyrrolidone and 180 mg of citric acid were dissolved in a water/ethanol mixture with a volume ratio of 5:3 at room temperature and the resultant solution was stirred at 80 °C for 10 min. Afterward, a certain amount of palladium nitrate was added to the above solution and the mixture was further stirred for 3 h to form the Pd precursor solution. A mixture of cerium nitrate/urea/citric acid with a molar ratio of 1:1:1 was dissolved in a water/n-butanol mixture with a volume ratio of 7:1 at room temperature and the resultant mixture was stirred for 20 min, afterward, a certain amount of hydrogen peroxide and Pd precursor solution were added (Pd theoretical loading was 1%). The final solution was sealed into an autoclave with a Teflon-lined, heated to 120 °C and maintained for a period of time. After hydrothermal treatment, the precipitate was centrifuged, washed with deionized water and ethanol repeatedly until pH $\approx$ 7, and subsequently dried at 60 °C for 7 h. The as-prepared powders were calcined in air at 400 °C for 4 h with a ramping rate of 1 °C min^{-1} and then treated at either 600 or 1000 °C for 2 h with the same heating rate. The obtained product was denoted as $H-Pd/CeO_2$-$T(t)$, where T represented the calcination temperature (T = 600, 1000 °C) and t stands for hydrothermal treatment time (t = 6, 12, 18, 24, 30 h). Amongst, the sample obtained under 24 h heat treatment was separately denoted as $H-Pd@CeO_2$-$T(24)$. For comparison, catalysts prepared by the impregnation method and coprecipitation method were denoted as $I-Pd/CeO_2$-T and $C-Pd/CeO_2$-T, respectively. Detailed synthesis methods are described in the Supporting Information.

4.2. Sample Characterization. SEM images were recorded using a Hitachi S-4800 electron microscope equipped with an energy dispersive X-ray detector. The acceleration voltage and working current was 5 kV and 7 μA, respectively. TEM images were performed on a FEI G2F30 transmission electron microscope at 300 kV. XRD measurement was carried out by a PANalytical Axios Petro diffractometer using X'Celerator detector and Cu Kα radiation (λ = 0.15406 nm, 45 kV and 40 mA). The XPS experiment was performed on a Thermo ESCALAB 250Xi spectrometer with Al Kα X-ray radiation (1486.6 eV), and all the binding energies were calculated using the C 1s peak as a reference at 284.8 eV. The XPS spectra were de-convoluted through a Gaussian/Lorentzian curve-fitting strategy. The content of Pd (or Ce) species with different valence states in the samples was obtained by calculating the relative integrated areas under the curve of each de-convoluted peaks.

CO pulse chemisorption, H_2-TPR and CO_2-TPD experiments of the catalysts (dosage: 100 mg) were all performed on a Micromeritics AutoChem 2920 instrument. For CO pulse chemisorption, before measurement, the sample was purged by helium gas at 300 °C to remove impurities and moisture for 30 min, then prereduced in a 10 vol % H_2/Ar flow (30 mL min^{-1}) at 300 °C for 1 h. Afterward, the measurements were performed when the sample was cooled down to 30 °C. In

the case of H$_2$-TPR, the sample was pretreated in the 3 vol % O$_2$/Ar flow (30 mL min^{-1}) at 400 °C for 40 min, and purged in He for 60 min, and then cooled to −30 °C with KWIKCOOL ASSEMBLY. The TPR profiles were monitored from −30 to 900 °C in 10 vol % H$_2$/Ar flow (30 mL min^{-1}) at a ramping rate of 5 °C min^{-1}. In the case of CO$_2$-TPD, the sample was pretreated under He (30 mL min^{-1}) at 300 °C for 1 h, and then cooled down to 50 °C, afterward, CO$_2$ flowed over the sample for 1 h. The measurement was carried out from 50 to 800 °C under He flow (30 mL min^{-1}) with a heating rate of 5 °C min^{-1}.

4.3. Catalytic Activity Test. The on-line analysis of catalytic activity for methane combustion was conducted using a continuous flow microreactor. The catalyst (0.045 g) was placed in a fixed-bed quartz reactor and the temperature of the catalyst bed was controlled by a K-type thermocouple. The fed gases containing 2 vol % CH$_4$, 4 vol % O$_2$, 20 vol % CO$_2$ and N$_2$ as balancing gas at a flow rate of 75 mL min^{-1}, were passed into the catalyst bed with a gas hourly space velocity (GHSV) of 100 000 mL h^{-1} g^{-1}. The inlet and outlet gas concentrations were analyzed with an on-line gas chromatograph fitted with a thermal conductivity detector. The CH$_4$ conversion (denoted as X) was calculated by the equation as follows

$$X = \frac{[CH_4]_{in} - [CH_4]_{out}}{[CH_4]_{in}} \times 100\%$$

where $[CH_4]_{in}$: the inlet flow of CH$_4$ and $[CH_4]_{out}$: the outlet flow of CH$_4$.

■ ASSOCIATED CONTENT

ⓢ Supporting Information

The Supporting Information is available free of charge on the ACS Publications website at DOI: 10.1021/acsomega.8b02556.

Synthesis of the I−Pd/CeO$_2$-T catalyst by the impregnation method; SEM images of catalysts; CO$_2$-TPD analysis and catalytic activity of the catalyst; CO pulse adsorption and XPS analysis (PDF)

■ AUTHOR INFORMATION

Corresponding Author
*E-mail: zhanyingying@fzu.edu.cn. Phone: +86 0591 83731234 ext. 8601. Fax: +86 0591 83709796 (Y.Z.).

ORCID ⓘ
Lilong Jiang: 0000-0002-0081-0367

Notes
The authors declare no competing financial interest.

■ ACKNOWLEDGMENTS

■ REFERENCES

(1) Chen, J.; Arandiyan, H.; Gao, X.; Li, J. Recent advances in catalysts for methane combustion. *Catal. Surv. Asia* **2015**, *19*, 140−171.
(2) Vickers, S. M.; Gholami, R.; Smith, K. J.; MacLachlan, M. J. Mesoporous Mn- and La-doped cerium oxide/cobalt oxide mixed metal catalysts for methane oxidation. *ACS Appl. Mater. Interfaces* **2015**, *7*, 11460−11466.
(3) Wang, S.; Zhao, C.; Li, S.; Sun, Y. First principles prediction of CH$_4$ reactivities with Co$_3$O$_4$ nanocatalysts of different morphologies. *Phys. Chem. Chem. Phys.* **2017**, *19*, 30874−30882.
(4) Horn, R.; Schlögl, R. Methane activation by heterogeneous catalysis. *Catal. Lett.* **2014**, *145*, 23−39.
(5) Tao, F. F.; Shan, J.-J.; Nguyen, L.; Wang, Z.; Zhang, S.; Zhang, L.; Wu, Z.; Huang, W.; Zeng, S.; Hu, P. Understanding complete oxidation of methane on spinel oxides at a molecular level. *Nat. Commun.* **2015**, *6*, 7798−7807.
(6) Ercolino, G.; Stelmachowski, P.; Specchia, S. Catalytic performance of Pd/Co$_3$O$_4$ on SiC and ZrO$_2$ open cell foams for process intensification of methane combustion in lean conditions. *Ind. Eng. Chem. Res.* **2017**, *56*, 6625−6636.
(7) Hu, W.; Li, G.; Chen, J.; Huang, F.; Gong, M.; Zhong, L.; Chen, Y. Enhancement of activity and hydrothermal stability of Pd/ZrO$_2$-Al$_2$O$_3$ doped by Mg for methane combustion under lean conditions. *Fuel* **2017**, *194*, 368−374.
(8) Chen, L.; McCann, J. P.; Tait, S. L. A re-examination of the catalyst activation and temperature hysteresis in methane combustion on Pt/Al$_2$O$_3$. *Appl. Catal., A* **2018**, *549*, 19−30.
(9) Wang, Y.; Arandiyan, H.; Scott, J.; Akia, M.; Dai, H.; Deng, J.; Aguey-Zinsou, K.-F.; Amal, R. High performance Au-Pd supported on 3D hybrid strontium-substituted lanthanum manganite perovskite catalyst for methane combustion. *ACS Catal.* **2016**, *6*, 6935−6947.
(10) Barbato, P. S.; Di Benedetto, A.; Di Sarli, V.; Landi, G.; Pirone, R. High-pressure methane combustion over a perovskite catalyst. *Ind. Eng. Chem. Res.* **2011**, *51*, 7547−7558.
(11) Xiao, Y.; Zhu, W.; Cai, G.; Chen, M.; Zheng, Y.; Zhong, F.; Jiang, L. Effects of A-site non-stoichiometry in Y$_x$InO$_{3+\delta}$ on the catalytic performance during methane combustion. *Phys. Chem. Chem. Phys.* **2017**, *19*, 30418−30428.
(12) Huang, F.; Wang, X.; Li, L.; Liu, X.; Xu, J.; Huang, C.; Zhang, T. Effect of magnesium substitution into Fe-based La-hexaaluminates on the activity for CH$_4$ catalytic combustion. *Catal. Sci. Technol.* **2016**, *6*, 7860−7867.
(13) Zheng, J.; Ren, X.; Song, Y.; Ge, X. Catalytic combustion of methane over iron- and manganese-substituted lanthanum hexaaluminates. *React. Kinet. Catal. Lett.* **2009**, *97*, 109−114.
(14) Zhu, G.; Han, J.; Zemlyanov, D. Y.; Ribeiro, F. H. The turnover rate for the catalytic combustion of methane over palladium is not sensitive to the structure of the catalyst. *J. Am. Chem. Soc.* **2004**, *126*, 9896−9897.
(15) Mihai, O.; Smedler, G.; Nylén, U.; Olofsson, M.; Olsson, L. The effect of water on methane oxidation over Pd/Al$_2$O$_3$ under lean, stoichiometric and rich conditions. *Catal. Sci. Technol.* **2017**, *7*, 3084−3096.
(16) Chen, X.; Zheng, Y.; Huang, F.; Xiao, Y.; Cai, G.; Zhang, Y.; Zheng, Y.; Jiang, L. Catalytic activity and stability over nanorod-like ordered mesoporous phosphorus-doped alumina supported palladium catalysts for methane combustion. *ACS Catal.* **2018**, *8*, 11016−11028.
(17) Eguchi, K.; Arai, H. Low temperature oxidation of methane over Pd-based catalysts-effect of support oxide on the combustion activity. *Appl. Catal., A* **2001**, *222*, 359−367.
(18) Willis, J. J.; Gallo, A.; Sokaras, D.; Aljama, H.; Nowak, S. H.; Goodman, E. D.; Wu, L.; Tassone, C. J.; Jaramillo, T. F.; Abild-Pedersen, F.; Cargnello, M. Systematic structure-property relationship studies in palladium catalyzed methane complete combustion. *ACS Catal.* **2017**, *7*, 7810−7821.
(19) Cai, W.; Yu, J.; Anand, C.; Vinu, A.; Jaroniec, M. Facile synthesis of ordered mesoporous alumina and alumina-supported metal oxides with tailored adsorption and framework properties. *Chem. Mater.* **2011**, *23*, 1147−1157.
(20) Murata, K.; Mahara, Y.; Ohyama, J.; Yamamoto, Y.; Arai, S.; Satsuma, A. The metal−support interaction concerning the particle size effect of Pd/Al$_2$O$_3$ on methane combustion. *Angew. Chem.* **2017**, *129*, 16209−16213.

(21) Zou, X.; Rui, Z.; Song, S.; Ji, H. Enhanced methane combustion performance over NiAl$_2$O$_4$-interface promoted Pd/γ-Al$_2$O$_3$. *J. Catal.* **2016**, *338*, 192−201.

(22) Yoshida, H.; Nakajima, T.; Yazawa, Y.; Hattori, T. Support effect on methane combustion over palladium catalysts. *Appl. Catal., B* **2007**, *71*, 70−79.

(23) Okumura, K.; Matsumoto, S.; Nishiaki, N.; Niwa, M. Support effect of zeolite on the methane combustion activity of palladium. *Appl. Catal., B* **2003**, *40*, 151−159.

(24) Abidli, A.; Hamoudi, S.; Belkacemi, K. Synthesis, character-ization and insights into stable and well organized hexagonal mesoporous zinc-doped alumina as promising metathesis catalysts carrier. *Dalton Trans.* **2015**, *44*, 9823−9838.

(25) Liao, H.; Liu, M.; Zuo, P. Preparation of Pd(Ce$_{1-x}$Y$_x$)O$_2$/γ-Al$_2$O$_3$/cordierite catalysts and its catalytic combustion activity for methane. *Catal. Commun.* **2016**, *76*, 62−66.

(26) Long, Y.; Song, S.; Li, J.; Wu, L.; Wang, Q.; Liu, Y.; Jin, R.; Zhang, H. Pt/CeO$_2$@MOF core@shell nanoreactor for selective hydrogenation of furfural via the channel screening effect. *ACS Catal.* **2018**, *8*, 8506−8512.

(27) Cargnello, M.; Doan-Nguyen, V. V. T.; Gordon, T. R.; Diaz, R. E.; Stach, E. A.; Gorte, R. J.; Fornasiero, P.; Murray, C. B. Control of metal nanocrystal size reveals metal-support interface role for ceria catalysts. *Science* **2013**, *341*, 771−773.

(28) Dai, Y.; Kumar, V. P.; Zhu, C.; MacLachlan, M. J.; Smith, K. J.; Wolf, M. O. Mesoporous silica-supported nanostructured PdO/CeO$_2$ catalysts for low-temperature methane oxidation. *ACS Appl. Mater. Interfaces* **2017**, *10*, 477−487.

(29) Hoffmann, M.; Kreft, S.; Georgi, G.; Fulda, G.; Pohl, M.-M.; Seeburg, D.; Berger-Karin, C.; Kondratenko, E. V.; Wohlrab, S. Improved catalytic methane combustion of Pd/CeO$_2$ catalysts via porous glass integration. *Appl. Catal., B* **2015**, *179*, 313−320.

(30) Guo, T.; Du, J.; Wu, J.; Wang, S.; Li, J. Structure and kinetic investigations of surface-stepped CeO$_2$-supported Pd catalysts for low-concentration methane oxidation. *Chem. Eng. J.* **2016**, *306*, 745−753.

(31) Chen, C.; Yeh, Y.-H.; Cargnello, M.; Murray, C. B.; Fornasiero, P.; Gorte, R. J. Methane oxidation on Pd@ZrO$_2$/Si-Al$_2$O$_3$ is enhanced by surface reduction of ZrO$_2$. *ACS Catal.* **2014**, *4*, 3902−3909.

(32) Melchionna, M.; Bracamonte, M. V.; Giuliani, A.; Nasi, L.; Montini, T.; Tavagnacco, C.; Bonchio, M.; Fornasiero, P.; Prato, M. Pd@TiO$_2$/carbon nanohorn electrocatalysts: reversible CO$_2$ hydro-genation to formic acid. *Energy Environ. Sci.* **2018**, *11*, 1571−1580.

(33) Wang, X.; Zhang, Y.; Song, S.; Yang, X.; Wang, Z.; Jin, R.; Zhang, H. L-Arginine-triggered self-assembly of CeO$_2$ nanosheaths on palladium nanoparticles in water. *Angew. Chem., Int. Ed.* **2016**, *55*, 4542−4546.

(34) Cargnello, M.; Jaen, J. J. D.; Garrido, J. C. H.; Bakhmutsky, K.; Montini, T.; Gamez, J. J. C.; Gorte, R. J.; Fornasiero, P. Exceptional activity for methane combustion over modular Pd@CeO$_2$ subunits on functionalized Al$_2$O$_3$. *Science* **2012**, *337*, 713−717.

(35) Adijanto, L.; Bennett, D. A.; Chen, C.; Yu, A. S.; Cargnello, M.; Fornasiero, P.; Gorte, R. J.; Vohs, J. M. Exceptional thermal stability of Pd@CeO$_2$ core-shell catalyst nanostructures grafted onto an oxide surface. *Nano Lett.* **2013**, *13*, 2252−2257.

(36) Li, L.; Zhang, N.; Huang, X.; Liu, Y.; Li, Y.; Zhang, G.; Song, L.; He, H. Hydrothermal stability of core-shell Pd@Ce$_{0.5}$Zr$_{0.5}$O$_2$/Al$_2$O$_3$ catalyst for automobile three-way reaction. *ACS Catal.* **2018**, *8*, 3222−3231.

(37) Zhu, W.; Jin, J.; Chen, X.; Li, C.; Wang, T.; Tsang, C.-W.; Liang, C. Enhanced activity and stability of La-doped CeO$_2$ monolithic catalysts for lean-oxygen methane combustion. *Environ. Sci. Pollut. Res.* **2017**, *25*, 5643−5654.

(38) Kang, W.; Ozgur, D. O.; Varma, A. Solution combustion synthesis of high surface area CeO$_2$ nanopowders for catalytic applications: reaction mechanism and properties. *ACS Appl. Nano Mater.* **2018**, *1*, 675−685.

(39) Zou, X.; Rui, Z.; Ji, H. Core-shell NiO@PdO nanoparticles supported on alumina as an advanced catalyst for methane oxidation. *ACS Catal.* **2017**, *7*, 1615−1625.

(40) Liu, F.; Zheng, X.; Chen, J.; Zheng, Y.; Jiang, L. Controlling the synthesis and application of nanocrystalline spherical and ordered mesoporous alumina with high thermal stability. *RSC Adv.* **2015**, *5*, 93917−93925.

(41) Song, S.; Li, K.; Pan, J.; Wang, F.; Li, J.; Feng, J.; Yao, S.; Ge, X.; Wang, X.; Zhang, H. Achieving the trade-off between selectivity and activity in semihydrogenation of alkynes by fabrication of (asymmetrical Pd@Ag Core)@(CeO$_2$ shell) nanocatalysts via autoredox reaction. *Adv. Mater.* **2016**, *29*, 1605332−1605337.

(42) Li, J.; Song, S.; Long, Y.; Wu, L.; Wang, X.; Xing, Y.; Jin, R.; Liu, X.; Zhang, H. Investigating the hybrid-structure-effect of CeO^{2-} encapsulated Au nanostructures on the transfer coupling of nitrobenzene. *Adv. Mater.* **2018**, *30*, 1704416−1704422.

(43) Dai, Q.; Bai, S.; Lou, Y.; Wang, X.; Guo, Y.; Lu, G. Sandwich-like PdO/CeO$_2$ nanosheet@HZSM-5 membrane hybrid composite for methane combustion: self-redispersion, sintering-resistance and oxygen, water-tolerance. *Nanoscale* **2016**, *8*, 9621−9628.

(44) Ciuparu, D.; Pfefferle, L. Support and water effects on palladium based methane combustion catalysts. *Appl. Catal., A* **2001**, *209*, 415−428.

(45) Gao, D.; Wang, S.; Zhang, C.; Yuan, Z.; Wang, S. Methane combustion over Pd/Al$_2$O$_3$ catalyst: effects of chlorine ions and water on catalytic activity. *Chin. J. Catal.* **2008**, *29*, 1221−1225.

(46) Wang, B.; Weng, D.; Wu, X.; Ran, R. Modification of Pd−CeO$_2$ catalyst by different treatments: Effect on the structure and CO oxidation activity. *Appl. Surf. Sci.* **2011**, *257*, 3878−3883.

(47) Slavinskaya, E. M.; Gulyaev, R. V.; Zadesenets, A. V.; Stonkus, O. A.; Zaikovskii, V. I.; Shubin, Y. V.; Korenev, S. V.; Boronin, A. I. Low-temperature CO oxidation by Pd/CeO$_2$ catalysts synthesized using the coprecipitation method. *Appl. Catal., B* **2015**, *166−167*, 91−103.

(48) Kaneko, K.; Inoke, K.; Freitag, B.; Hungria, A. B.; Midgley, P. A.; Hansen, T. W.; Zhang, J.; Ohara, S.; Adschiri, T. Structural and morphological characterization of cerium oxide nanocrystals prepared by hydrothermal synthesis. *Nano Lett.* **2007**, *7*, 421−425.

(49) Ma, J.; Lou, Y.; Cai, Y.; Zhao, Z.; Wang, L.; Zhan, W.; Guo, Y.; Guo, Y. The relationship between the chemical state of Pd species and the catalytic activity for methane combustion on Pd/CeO$_2$. *Catal. Sci. Technol.* **2018**, *8*, 2567−2577.

(50) Lei, Y.; Li, W.; Liu, Q.; Lin, Q.; Zheng, X.; Huang, Q.; Guan, S.; Wang, X.; Wang, C.; Li, F. Typical crystal face effects of different morphology ceria on the activity of Pd/CeO$_2$ catalysts for lean methane combustion. *Fuel* **2018**, *233*, 10−20.

(51) Guo, Y.; Lu, G.; Zhang, Z.; Zhang, S.; Qi, Y.; Liu, Y. Preparation of Ce$_x$Zr$_{1-x}$O$_2$ (x=0.75, 0.62) solid solution and its application in Pd-only three-way catalysts. *Catal. Today* **2007**, *126*, 296−302.

(52) Xia, X.; Figueroa-Cosme, L.; Tao, J.; Peng, H.-C.; Niu, G.; Zhu, Y.; Xia, Y. Facile synthesis of iridium nanocrystals with well-controlled facets using seed-mediated growth. *J. Am. Chem. Soc.* **2014**, *136*, 10878−10881.